Materials Characterization 128 (2017) 217–225

Contents lists available at ScienceDirect

Materials Characterization

journal homepage: www.elsevier.com/locate/matchar

Multiscale in situ deformation experiments: A sequential process from strain localization to failure in a laminated Ti-6Al-4V alloy

Motomichi Koyama[a,*], Keita Yamanouchi[a], Qinghua Wang[b], Shien Ri[b], Yoshihisa Tanaka[c], Yasuaki Hamano[a], Shigeto Yamasaki[d], Masatoshi Mitsuhara[d], Masataka Ohkubo[e], Hiroshi Noguchi[a], Kaneaki Tsuzaki[a]

[a] Department of Mechanical Engineering, Kyushu University, Motooka 744, Fukuoka 819-0395, Japan
[b] Research Institute for Measurement and Analytical Instrumentation, National Institute of Advanced Industrial Science and Technology, 1-1-1 Umezono, Tsukuba 305-8568, Japan
[c] National Institute for Materials Science, 1-2-1 Sengen, Tsukuba 305-0047, Japan
[d] Department of Engineering Sciences for Electronics and Materials, Kyushu University, 6-1 Kasuga Koen, Kasuga, Fukuoka 816-8580, Japan
[e] Nanometronics Lab for Structural Materials, National Institute of Advanced Industrial Science and Technology, 1-1-1 Umezono, Tsukuba 305-8568, Japan

ARTICLE INFO

Keywords:
In situ
Titanium
Lamella
Dual phase
Strain localization
Sampling moiré

ABSTRACT

The microscopic factors causing tensile failure of an α/β laminated Ti-6Al-4V alloy were investigated through in situ scanning electron microscopy and sampling moiré at an ambient temperature. Specifically, multiscale in situ microscopic observations were conducted to extract the most crucial factor of the failure. Slip localization in the vicinity of an intergranular α-sheet was clarified to be the primary factor that causes failure of the Ti-6Al-4V alloy. In addition, no relationship between interfacial strain localization and macroscopic shear localization at 45 degrees against the tensile direction was observed.

1. Introduction

Laminated microstructures have played an important role on the enhancement of mechanical properties such as tensile strength [1], toughness [2], and fatigue crack resistance [3]. Superior tensile properties have been reported in metal laminated microstructures, e.g., pearlitic steels [4,5], transformation-induced plasticity maraging steel [6,7], and nanotwinned copper [8,9]. Therefore, utilization of the laminated microstructures is expected to provide a breakthrough for the design strategy of high strength structural materials.

In addition to the metal materials mentioned above, titanium alloys also show an α/β (HCP/BCC: hexagonal close-packed and body centered cubic structures) laminated microstructure. In fact, the α/β lamella is an initial microstructure of an as-β-solution-treated Ti-6Al-4V (wt%) alloy that is the most practical alloy composition [10,11]. Because of its low density and high corrosion resistance in addition to its high strength, the laminated Ti-6Al-4V alloy has been used for automobile parts such as engine bulbs. Therefore, deformation mechanisms of the laminated Ti-6Al-4V alloy are important in uncovering intrinsic factors that affect its mechanical properties.

From the viewpoint of deformation characteristics-mechanical property relation in Ti-6Al-4V alloys, the local plastic strain evolution and associated damage formation play important roles on fatigue resistance [12,13], wear [14], machinability [15], and tensile properties [16–18]. Specifically, grain/phase interfaces and lamella morphologies have played important roles on plastic strain localization, which can be a primary factor that affects the micromechanism of the damage formation. In fact, the laminated Ti-6Al-4V alloy has also been reported to show damage formation along a microstructural interface [19]. However, to the best of our knowledge, an underlying mechanism of the interfacial damage evolution mechanism in the laminated Ti-6Al-4V alloy has not been clarified experimentally in terms of microstructural plastic strain localization.

To visualize the sequential process from strain localization to damage formation, in situ microscopic observations have been widely recognized as one of the most powerful techniques [20–22]. In particular, surface relief and distortion have been directly correlated with damage formation under in situ observations [23–25]. This study aims to elucidate the effects of plastic strain evolution on damage formation in terms of the macroscopic strain path, microstructural strain localization, and interface characteristics.

* Corresponding author.
E-mail address: koyama@mech.kyushu-u.ac.jp (M. Koyama).

http://dx.doi.org/10.1016/j.matchar.2017.04.010
Received 24 November 2016; Received in revised form 28 March 2017; Accepted 8 April 2017
Available online 09 April 2017

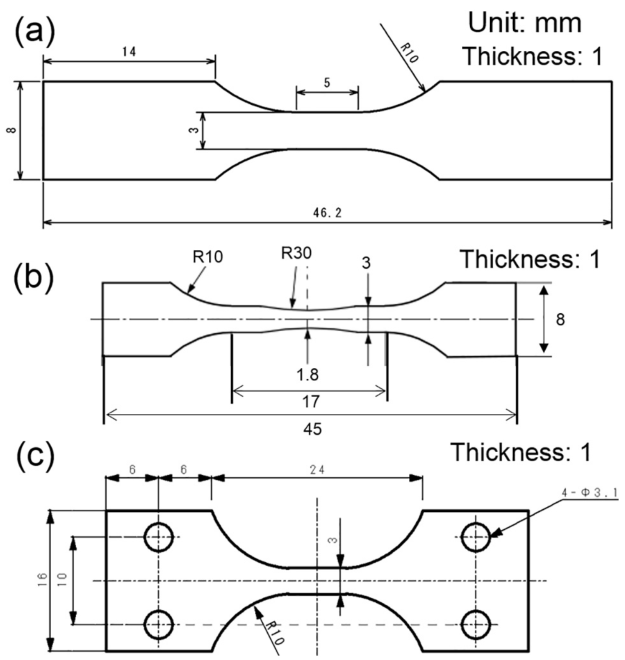

Fig. 1. Specimen geometries for (a) tensile testing, (b) in situ strain mapping through the sampling moiré, and (c) in-situ observations of surface relieves.

2. Experimental Procedure

2.1. Material

We received a Ti-6.29Al-4.35V-0.155O-0.225Fe alloy billet with a dimension of 245 mm in diameter and 360 mm in length produced by melting and subsequent hot working. A β-solution heat treatment was performed at 1323 K for 1.5 h and subsequently water-quenched. The heat-treated sample was annealed at 973 K for 3 h and air-cooled to remove the residual stress. Specimens for mechanical testing and in situ testing were cut by spark machining and subsequently mechanically polished. The specimen geometries are shown in Fig. 1. Since spark machining introduces hydrogen into the specimen surfaces, specimen surface layers with a thickness of 1 mm on both sides were removed by mechanical polishing. Tensile deformations were provided at an ambient temperature and a nominal strain rate of $3 \times 10^{-4}\,s^{-1}$.

2.2. Strain Mapping Through Sampling Moiré

In this study, we applied the sampling moiré method [26] to measure the displacement and strain distributions of a Ti alloy. A cross grating with the pitch of 3 μm was fabricated on the specimen surface by ultraviolet (UV) nanoimprint lithography (EUN-4200 device). The UV wavelength was 375 nm and the UV illumination time was 30 s. The specimen was loaded using a self-developed automatic tensile device under a laser scanning microscope (OPTELICS HYBRID). The tensile direction was parallel to axial direction. We captured the grating images under different tensile loads during deformation by use of the laser scanning microscope.

In the sampling moiré method, after image processing using 4-pixel down-sampling and intensity interpolation [27] techniques for each grating image, multiple phase-shifted moiré fringes were simultaneously generated. Then, the phase distributions of the moiré fringes under different loads were determined by the phase-shifting technique. Next, the phase differences between the moiré fringes before and after deformation allowed us to determine the two-dimensional in-plane displacement distributions accurately. Subsequently, the normal strains in the axial and transverse directions and the shear strain were calculated from the first-order partial derivatives of the two-dimensional displacements [28] with the filter size of 12 × 12 pixels (three times the down-sampling pitch). Finally, the maximum principal strain distributions were measured from the analysis of strain status for plane stress problems based on the full-field normal and shear strains.

2.3. In Situ Observation of Surface Relieves and Post-mortem Analysis

To observe slip/damage evolutions at multiple scales corresponding to respective microstructure sizes simultaneously, the in situ observations were carried out with different magnifications in an identical location by using a micro-tension machine (Gatan: MTEST5000) equipped with a secondary electron microscope (SEM). Precise strains during the in situ observations were directly measured by using low magnification images. The tensile deformations were provided at an ambient temperature and a nominal strain rate of $3 \times 10^{-4}\,s^{-1}$.

Secondary electron (SE) imaging was conducted at 15 kV. For the SE imaging, the specimen surface was etched by a chemical solution of $HF:HNO_3:H_2O$ = 1:2:47. To avoid the effects of creep deformation, all of the SE images were taken after unloading. In addition, electron backscatter diffraction pattern (EBSD) measurements with an accelerating voltage of 15 kV were carried out at a beam step size of 1 μm, 0.2 μm or 50 nm. The EBSD measurements with the beam step size of 1 μm and 0.2 μm were conducted on a mechanically polished surface. The specimen for the high spatial resolution EBSD analysis with the beam step size of 50 nm was prepared by mechanically polishing and subsequent electrochemical polishing in a solution of 5%H_2SO_4 and 95%CH_3OH. In addition, scanning transmission electron microscopic (STEM) observations were carried out at an acceleration voltage of 400 kV. The specimen for the STEM observation was prepared by using focused ion beam. In observations regions for the high resolution EBSD and STEM, elemental mapping was also conducted by energy dispersive X-ray spectrometry (EDS).

3. Results

3.1. Initial Microstructure

Fig. 2a shows an SE image of an initial microstructure. The microstructure is fully laminated, which has been known to consist of α and β phases [10]. A thin microstructure is located along the prior β grain boundaries, as indicated by the white arrows. Here, prior β grain boundaries were identified as the ones surrounding equiaxial grains which were chemically etched clearly. This microstructure has been conventionally referred to as fully lamellar microstructure [12]. The majority of the constituent phase is α. β-films are extremely thin in the present alloy; therefore, the plates are not identified as β-phase in the overview EBSD image shown in Fig. 2b and are instead identified as the same phase and orientation as the surrounding α-phase. The β films can be clearly visualized by backscattered electron (BSE) imaging (Fig. 3a) coupled with high resolution EBSD phase mapping (Fig. 3b). As indicated by Fig. 3c, vanadium and oxygen are enriched in β films. Because of the elemental partitioning, a high angle annular dark field (HAADF) image shown in Fig. 3e clearly demonstrates the α/β laminated microstructure. A thickness of the β films observed in the TEM images is 20–80 nm. An average prior β grain size, a colony size, an average α lamellae lath thickness were 1.1 mm, 400 μm, and 1.1 μm, respectively.

In addition, the inverse pole figure (IPF) maps shown in Fig. 2b indicates that the thin microstructure along the grain boundaries is also α-phase. Hereafter, the laminated α/β matrix and the α-phase at prior β grain boundaries are referred to as the α lath block and the intergranular α-sheet, respectively. In addition, the group of α + β region consisting of the same lamellar alignment is refer to as α lath colony.